New Approaches for Monitoring Image Data

Yarema Okhrin, Wolfgang Schmid, and Ivan Semeniuk

***Abstract*— In this paper, we develop new techniques for monitoring image processes under a fairly general setting with spatially correlated pixels in the image. Monitoring and handling the pixels directly is infeasible due to an extremely high image resolution. To overcome this problem, we suggest control charts that are based on regions of interest. The regions of interest cover the original image which leads to a dimension reduction. Nevertheless, the data are still high-dimensional. We consider residual charts based on the generalized likelihood ratio approach. Existing control statistics typically depend on the inverse of the covariance matrix of the process, involving high computing times and frequently generating instable results in a high-dimensional setting. As a solution of this issue, we suggest two further control charts that can be regarded as modifications of the generalized likelihood ratio statistic. Within an extensive simulation study, we compare the newly proposed control charts using the median run length as a performance criterion.**

***Index Terms*— Control chart, digital image processing, high-dimensional data, median run length, regions of interest, statistical process control.**

I. Introduction

IMAGES play an increasingly important role not only in social media but also in all phases of manufacturing, particularly within Industry 4.0. The key objective when analyzing images is to extract meaningful and useful information (mainly from digital images) with the aim of aggregating and improving image data for further processing. This covers such tasks as the storage, compression, and extraction of pictorial information (cf. [1]), and is typically done by means of digital image processing techniques. Since the resolution of digital cameras has dramatically increased in recent years and the possible applications of images are heterogeneous, a new strand of research that tackles the analysis of image data with statistical tools has evolved.

To build a statistical model for a sequence of images, we assume that the pixels constituting the images can be understood as a realization of a stochastic process. This is attained by quantifying each pixel by its coordinates, color, and intensity, and results in a time series of multivariate spatial data. Numerous statistical approaches such as, e.g., Kalman filtering, Markov random fields, hidden Markov processes, and Bayesian approaches have recently been customized to model image processes. An excellent overview can be found in, e.g., [2]. The objectives of the image analysis typically involve the overcoming of issues with feature extraction, image classification, image transformation, etc. Modern cameras can produce images with high resolutions, involving high-dimensional data sets. Thus, the statistical techniques to be applied must be capable of handling and modelling large and specifically structured data.

The key goal, both from theoretical and practical perspectives, is to monitor an image process over time and detect changes, which may be indicative of faults, as soon as possible after their occurrence. Such problems arise frequently in many fields of application, e.g., production processes, medicine, environmental science, etc. Nowadays, the quality control procedures involved in production processes employ new measurement methods that are aimed at detecting faulty products, e.g., the sensors that take regular photos of the items under production. Reference [3] considers the application of quality control procedures in a 3D printing process. Issues involving changes to the image process can also be observed in the media and advertising industries, in which it is essential to control the quality of printed materials, for example, their brightness. To ensure quality, the cover of a magazine could, for example, be checked for changes. There are also many scenarios in medicine in which it is essential to swiftly detect image changes, such as the early detection of tumors, vascular changes, etc. In all these applications, those responsible for monitoring the image process aim to detect any deviations from what is expected to be normal as soon as possible after their occurrence. High quality image processing results in less defective products, prettier magazines, earlier diagnoses, etc.

An excellent overview of control charts for images is given in [4]. Reference [5] was the first to apply control charts to image data; their purpose was to improve the productivity of web applications. In [6], illumination changes through a transformation of the pixel values of the image were taken into account. The authors constructed individual moving-range control charts for each pixel. A disadvantage of their approach, however, is that the correlation structure of neighboring pixels is not taken into account. Reference [7] combined control charts for variable data with the EWMA control chart. Hotelling's T^2 control chart has been widely applied in image analysis, e.g., by [8]–[10]. References [11] and [12] combined multivariate control charts and wavelets to detect defects in electronic components. Reference [13] compared a wavelet and Hotelling's T^2 control chart with a wavelet and a principal component approach to detect defects in LED chips. Reference [14] utilized a spatially exponentially weighted moving average chart to find defects in

Manuscript received May 7, 2020; revised October 7, 2020; accepted November 10, 2020. Date of publication November 25, 2020; date of current version December 8, 2020. The associate editor coordinating the review of this manuscript and approving it for publication was Dr. Chun-Shien Lu. *(Corresponding author: Yarema Okhrin.)*

Yarema Okhrin is with the Department of Statistics, University of Augsburg, 86159 Augsburg, Germany (e-mail: yarema.okhrin@wiwi.uni-augsburg.de).

Wolfgang Schmid and Ivan Semeniuk are with the Department of Statistics, European University Viadrina, 15230 Frankfurt (Oder), Germany.

Digital Object Identifier 10.1109/TIP.2020.3039389

LCD monitors, while [15] employed a spatial $\bar{x}$ chart for the same application. In [16], a nonparametric regression method using wavelet basis functions was developed to extract features from grayscale image data. The extracted features were monitored over time to detect out-of-control observations using a generalized likelihood ratio control chart. In further studies, methods of machine learning have been applied to monitor image processes. For example, [17] applied the K-medoids clustering algorithm for colored RGB images.

Recently, [18] proposed a deep belief network for feature extraction and timely fault detection in industrial image processes. For the purposes of their studies, the authors built sub-networks to extract local features from sub-images. In a more classical setting, [19] proposed a data-driven in situ monitoring method using a kernel density estimation-based Hotelling's T^2 control chart to detect unstable melting conditions during the selective laser melting of zinc powder; their method of detection was applied to thermal image streams containing plume emission information. This approach was further explored in [20]. Reference [21], meanwhile, presented a profile monitoring method for image data in the context of fused deposition modeling. A similar problem was tackled in [22], where the authors relied on the generalized likelihood ratio method.

This paper contributes to the current literature in many directions. First, we assume that the pixels exhibit a spatial dependence and that their corresponding characteristics are not independent; this is contrary to the assumptions that are typical in the literature. We quantify their dependency using a spatial covariance matrix that can be flexibly set or estimated from historical data. Second, since modern cameras produce high-resolution images but it is not computationally feasible to deal separately with every pixel of an image, we work with regions of interest (ROIs), i.e., fixed geometric areas that cover the whole image and significantly reduce the dimensionality. The stochastic properties of the ROIs are derived, in this paper, directly from the model for the pixels, while the shape and size of the ROIs can be arbitrary. We go on to suggest two alternative versions of settings with non-overlapping and overlapping ROIs. Third, even with the implementation of the ROIs, the final dimension of the monitored data is high and it can be unstable and computationally demanding to estimate the inverse covariance matrix using historical data. Therefore, we offer three new control schemes that are based on the generalized likelihood ratio test (GLR). The aim of the schemes is to detect a location shift in the color of a grayscale image. Two of the three suggested schemes are modified and depend on the covariance matrix only, and not on its inverse. This leads to great advantages in applications.

To summarize, this paper contributes to the field, since we:

- derive new control charts for monitoring changes in image data;
- suggest methods that can be applied to high-resolution images;
- take spatial correlation of pixels into account and suggest methods for simulating such data;
- outperform the benchmark Hotelling's T^2 control chart using Median Run Length as a performance criterion.

The paper is structured as follows. In Section II, we provide a brief introduction for image analysis and statistical image analysis. We also explain the statistical model to be employed in the rest of the paper. In Section III, we develop the control charts and discuss the high-dimensional nature of the underlying problem in detail. Section IV provides a comparison study of the procedures discussed in Section III, in which we treat several out-of-control situations. The concluding notes are given in Section V.

II. Statistical Image Analysis

In this section, we briefly describe some basic concepts of image analysis focusing on statistical image processing. More details can be found in, e.g., [1], [2], [23], and [24].

Each 2-dimensional image can be defined as a function $f : D \to W$, where $D \subset \mathbb{R}^2$ and $W \subset \mathbb{R}^k$. Typically, D is a rectangle. The k dimension defines the technical complexity of the image. For a black-white image, $k = 1$ and W consists of only two values, 0 and 1 (usually with 0 standing for black and 1 for white color). Larger values of k are required to represent color images. If we adopt the RGB (red, green, blue) convention, then $k = 3$ and $f(x, y)$ is a vector of three individual components. For an 8-bit image, these components take integer values between 0 and $2^8 - 1 = 255$ (cf. [24]). If all elements are equal to zero, then we obtain a black image; if all are equal to 255, then the resulting image is white. Nowadays, most high-quality images are 24-bit or 32-bit, and, thus, they involve a much wider variety of colors, i.e., 2^{24} or 2^{32}, respectively. To standardize the operation of image processing on different images, their values are typically rescaled to $[0, 1]$. If all the components are set to be equal, which is equivalent to downgrading the function to $k = 1$, then we obtain a grayscale image. In the following sections, we will exclusively deal with grayscale images, though the methodology can be directly extended to the case with color images.

A digital image, contrary to a non-digital one, consists of a discrete set of pixels. Every pixel is not a single point in $\mathbb{R}^2$ but is, in fact, a rectangular area. Thus, in order to process an image, it must be represented by a discrete data structure. Formally speaking, a digital image can be obtained from an image by sampling and quantization (e.g., [1], [24]). More precisely, an image is defined as $f(i\Delta x, j\Delta y)$ for $i = 1, \ldots, l,\ \ j = 1, \ldots, p$, where Δx and Δy are the geometric length and width of the area of interest, e.g., of a pixel. The locally constant function, f, is known as the intensity function and its values are the intensities of the corresponding areas/pixels. To shorten the notation, we write f_{ij} instead of $f(i\Delta x, j\Delta y)$ and refer to a digital image simply by using the word, "image". An image with l rows and p columns of pixels can be written as an array,

$$\begin{bmatrix} f_{11} & \cdots & f_{1p} \\ f_{21} & \cdots & f_{2p} \\ \vdots & \ddots & \vdots \\ f_{l1} & \cdots & f_{lp} \end{bmatrix}.$$

In practice, the size of the array can be large. The resolution of images taken by high-end smartphones can reach 4032×3024 pixels, leading to enormous arrays.

Images taken by a camera and discretized by the intensity function can suffer from several sources of error. These are caused, for instance, by pure light measurement errors, various technical issues, changes in the lighting, particles in the air, the instability of the object, etc. Furthermore, the use of quantization as a smoothing technique introduces additional noise into the image. Thus, an image could be treated as a realization of a stochastic process, in a similar manner to the measurement error models in statistics. In the following sections, we consider a linear error model in which only an additive noise influences the pixel intensities, f_{ij}. The latter is commonly referred to as the nominal image in the literature. In practice, the nominal image serves as the target value of the image and is contaminated by noise caused by the peculiarities of the production process. This results in the observed image, $\tilde{Y}_{ij}$. More precisely,

$$\tilde{Y}_{ij} = f_{ij} + \varepsilon_{ij}, \quad i = 1, \ldots, l, \;\; j = 1, \ldots, p. \tag{1}$$

We assume that the nominal intensities $\{f_{ij}\}$ and the error variables $\{\varepsilon_{ij}\}$ are orthogonal. Regarding the distribution of the error terms, the current literature appears to impose a homogeneous assumption that the random variables ε_{ij}, $i = 1, \ldots, l$, $j = 1, \ldots, p$ are spatially independent and normally distributed with mean 0 and variance σ^2. This is the case, usually, when the image has been pre-processed; the error quantities explain the deviation between the observed pixel intensities and the smoothed values. This is obviously not a valid assumption in many applications and is often seen to be restrictive. The authors of [1] describe several cases where this approach does not work (e.g., quantum-limited imaging, such as in X-ray, nuclear-medicine imaging, etc.).

In this paper, we consider a more general model and, thus, relax the independence assumption. We utilize the matrix-valued normal distribution assuming certain types of covariance matrices, as is done in spatial statistics (cf. [25]). Consequently, the pixel intensity process is spatially correlated. This approach fosters a more realistic representation of the true data–generating process for digital images.

III. Monitoring Procedures for Image Characteristics

In this research paper, we develop methods for the surveillance of image processes over time. These types of problems are common in practice and arise in many fields. Modern production processes, for instance, frequently deploy cameras as sensors to continuously monitor quality. The objects of interest are either the items under production or, in a more specific case, parts created from a 3D printing process (cf. [3]). Similarly, one can consider the printing process of magazines, books or flyers, during which the intensity and the color of the cover might be monitored. In medicine, screening generates sequences of spatial or temporal images, which are reviewed for the early detection of tumors and vascular changes. In another example, the airspace above us can be monitored by the military for the detection of foreign aircrafts, while down from above, the surveillance of satellite pictures can help in the timely detection of forest fires. Thus, the number of possible applications for the surveillance of image processes over time are diverse, though related research is still at an early stage.

All time series data can be modelled and analyzed in the domains of time or frequency, thus offering two methodological alternatives. In this work, we focus on monitoring procedures in the time domain only. In the frequency domain, the time series of image characteristics would first need to be transformed by a suitable filter, for example, wavelets, etc. This can lead, however, to difficulties in the interpretation of changes, in the context of the original image, that result due to transformational process. We will not discuss the topic further here.

The aim of any monitoring procedure is to detect a shift in the observed process as soon as possible after its occurrence. Such a problem is subject to statistical process control (SPC, cf. [26]). The most important tools in SPC are control charts, which have been widely employed in engineering, as well as in other fields, such as production, economics, medicine, etc. The process of interest is mostly assumed to be univariate and independent over time. If there is a need to monitor several characteristics of a process, the resulting time series is then a multivariate time series. Control charts for multivariate processes and those that are independent over time have been studied by various authors. The first control chart for independent and multivariate normally distributed random vectors was suggested by [27]. Instead of monitoring the vector of the observations, the author suggested to consider the scalar Mahalanobis distance between the observations and the target mean vector. References [28] and [29] extended the exponentially weighted moving average (EWMA) chart to multivariate data by developing a multivariate EWMA recursion. Further generalizations of the EWMA chart were then given by, e.g., [30] and [31]. The alternative family of control charts stem from the sequential probability ratio test (SPRT) and are referred to as cumulative sum (CUSUM) charts. The extension of the univariate CUSUM scheme to multivariate data is not unique; several alternative approaches have been developed. The direct application of the SPRT to independent multivariate normally distributed variables results in a control chart that is not directionally invariant (cf. [32]). This implies that the distribution of the run length in an out-of-control state is dependent on the direction and on the magnitude of the change. As a result, the application of the charts becomes very problem-driven and computationally expensive. Several authors have, therefore, proposed control schemes that overcome this problem, e.g., [33], [34].

Unfortunately, these approaches cannot be applied to monitor an image process directly. Despite being capable to monitor multivariate time series data, these charts can handle only small- and medium-dimensional data. As image data renders ultra-high-dimensional time series containing potentially millions of dimensions, it is necessary either to modify these approaches or to introduce new ones.

One potential method for reducing dimensionality of the problem is to consider aggregated characteristics of the

image-based processes such as, e.g., entropy, spatial entropy, and means, rather than monitoring every pixel. The information can be aggregated spatially over pixels or in a pixel-specific way. The disadvantage of a pixel-to-pixel analysis is that it creates dramatic theoretical and computational problems. Particularly, since we assume there are correlated pixels within an image, such an analysis can only be successful if the underlying covariance matrix of the pixels has a specific structure. Otherwise, the number of parameters with respect to the available amount of data would be huge and the analysis would suffer from the curse of dimensionality.

Spatial-aggregation relies on sub-images, the so-called regions of interest (ROIs), as considered in [16], [35]. These are obtained by splitting the whole image into small areas of a given geometric form and of either a fixed or varying size. The local characteristics of the ROIs usually comprise measures of location and local measures of variation in colors or intensities. Our aim, in this paper, is to monitor such local characteristics. The introduction of sub-images reduces the dimensionality of the data, though it can lead to new problems. Nevertheless, we are still faced with a high-dimensional problem and the classical control charts for multivariate processes cannot be applied.

In order to develop efficient control charts, the methods for multivariate process control must be combined with the latest findings on high-dimensional data analysis and on spatio-temporal statistics.

A. Model

Our aim is to detect whether there has been a change within an image process over time. Let $\tilde{Y}_{t,ij}$ be the true intensity of the pixel with coordinates (i, j) at time $t \geq 1$. Since the image process may be quite complicated, in this paper we focus on a situation where the nominal image, defined by the intensities f_{ij}, is fixed and does not change over time. For instance, the image could be the template of a book cover, as modelled on a computer or taken by a static camera as part of the printing process. The objective of monitoring the process is then to detect changes in the brightness of continuously printed book covers. This implies that the intensity f_{ij} is constant for the given pixel (i, j) and independent of time t. The linear error model, therefore, becomes as follows

$$\tilde{Y}_{t,ij} = f_{ij} + \varepsilon_{t,ij}, \quad i = 1, \ldots, l, \quad j = 1, \ldots, p, \tag{2}$$

where the elements $\tilde{Y}_{t,ij}$ constitute a matrix $\tilde{\mathbf{Y}}_{\mathbf{t}}$. A more general case of a non-constant nominal image, and therefore time dependent intensity functions, is discussed in an ongoing separate project. The quantity $\varepsilon_{t,ij}$ denotes a noise process that is assumed to be independent over time but not over space, i.e., $Corr(\varepsilon_{t,ij}, \varepsilon_{s,i'j'}) = 0$ for $t \neq s$, but $Corr(\varepsilon_{t,ij}, \varepsilon_{t,i'j'}) \neq 0$ in general. Thus, we are working under much weaker assumptions than are usually held in the literature, whereby independence over space is largely assumed.

Since we are considering a shift in the location, the change point model is defined as

$$\tilde{\mathbf{X}}_t = \begin{cases} \tilde{\mathbf{Y}}_t & \text{for } t < \tau, \\ \tilde{\mathbf{Y}}_t + \mathbf{A} & \text{for } t \geq \tau \end{cases} \tag{3}$$

for $t \geq 1$ with $\mathbf{A} \neq \mathbf{0}$ and $\tau \in \mathbb{N} \cup \{\infty\}$. If $\tau = \infty$, we determine that the image process is in control and no change has happened. If $\tau < \infty$, then a shift has occurred and the image process is out of control, starting from time point τ. $\{\tilde{\mathbf{X}}_t\}$ is frequently referred to as the observed process and $\{\tilde{\mathbf{Y}}_t\}$ as the target process. Note that f is assumed to be known and we do not need a pre-run phase to estimate it. Although in many applications there are no natural values for the in-control characteristics, here we can assume that there exists a template that can be utilized as the nominal image. The impacts of parameter estimation will be discussed in a forthcoming paper.

Monitoring all pixels individually is a very challenging task, since a simple modern cell phone image consists of around four million pixels, thus, we would have to monitor a process with four million components over time, which is not feasible from a computational perspective. In order to reduce the complexity of the problem, the image is partitioned into ROIs I_{ij} of size $h_1 \times h_2$, $i = 1, \ldots, r_1$, $j = 1, \ldots, r_2$. We distinguish between the cases of non-overlapping and overlapping ROIs. In the first case, one can assume that $l = h_1\, r_1$ and $p = h_2\, r_2$, $r_1, r_2 \in \mathbb{N}$ and $I_{ij} \cap I_{i'j'} = \emptyset$, whereas, for the second case, $l < h_1 \cdots r_1$, $p < h_2\, r_2$ and $I_{ij} \cap I_{i'j'} \neq \emptyset$. ROIs often set as squares with $h_1 = h_2$. As suggested in [35], ROIs can instead be considered not to be of a fixed size but to represent an increasingly nested sequence of regions, i.e., $I_1 \subset I_2 \subset \ldots$. While the methodology discussed in this paper could easily be extended to such a setting, to simplify the exposition, we restrict the discussion to overlapping and non-overlapping ROIs of a fixed size.

Every ROI consists of a set of pixels and the intensities of the pixels must be aggregated to the local characteristics of the ROIs. Most of the proposed charts are based on characteristics $\tilde{T}_{t,ij}$ of the pixel intensities within a given ROI I_{ij} such as the mean, weighted mean, standard deviation, etc. We follow the same idea as [35] and [36], who have applied a control chart to the residual process. In these studies, the authors monitored the mean of the pixels within every ROI using a generalized likelihood ratio chart. It must be noted that their approach assumes spatial independence between the pixels, though, even in the case of a multiple linear regression, the residual process is not independent. A detailed comparison of residual charts and so-called modified charts is given in [37].

B. Control Charts Based on the GLR Approach

In this part of the article, we introduce some new control procedures for image characteristics. While in most published papers, their analysis is restricted to the characteristics of the spatially independent residual process for the independent ROIs, we take into account the spatial structure (thus, the dependence) of the pixels. Consequently, we are able to monitor the characteristics of the original image, too.

The non-overlapping ROIs are built, as in the previous subsection, resulting in a total of $r_1 \cdot r_2$ ROIs. Let $\tilde{T}_{t,ij}$ denote a local characteristic of the image process for the region I_{ij} such as, e.g., the local mean $\tilde{T}_{ij} = \bar{X}_{t,ij} = \frac{1}{|I_{ij}|} \sum_{(v,u) \in I_{ij}} \tilde{X}_{t,vu}$, the median, the entropy of the observations lying in I_{ij}, etc.

To simplify the formulas and the notation, and taking into account the fact that there are no further constraints on the arrays, we define $\mathbf{X}_t$ as the vectorized version of the $l \times p$ matrix $\tilde{\mathbf{X}}_t$. Thus, $\mathbf{X}_t = \left(\tilde{X}_{t,11}, \tilde{X}_{t,21}, \ldots, \tilde{X}_{t,l1}, \ldots, \tilde{X}_{t,lp}\right)' = \mathrm{vec}(\tilde{\mathbf{X}}_t)$. We assume that the observed intensities in the in-control state follow an $l \cdot p$-dimensional normal distribution $\mathbf{X_t} \sim N_{l\cdot p}(\boldsymbol{\mu}_X, \Sigma_X)$ with the mean vector $\boldsymbol{\mu}_X$ and the covariance matrix $\boldsymbol{\Sigma}_X$. Moreover, the characteristics of the ROIs $\mathbf{T}_t = (\tilde{T}_{t,11}, \tilde{T}_{t,21}, \ldots, \tilde{T}_{t,r_1 1}, \ldots, \tilde{T}_{t,r_1 r_2})'$ are assumed to follow a multivariate normal distribution with mean $\boldsymbol{\mu}$ and covariance matrix $\mathbf{G}$. Note that $\boldsymbol{\mu}$ is an $r_1 \cdot r_2$-dimensional vector and $\mathbf{G}$ is an $(r_1 \cdot r_2) \times (r_1 \cdot r_2)$–dimensional matrix. If $\tilde{T}_{t,ij}$ are means of the pixel intensities, then we can state that $E(\tilde{T}_{ij}) = \frac{1}{|I_{ij}|} e'_{ij} \boldsymbol{\mu}_X$ and $Var(\tilde{T}_{t,ij}) = \frac{1}{|I_{ij}|^2} e'_{ij} \Sigma_{\mathbf{X}} e_{ij}$, where e_{ij} is an $l \cdot p$ vector of zeros and ones made by vectorization of the $l \times p$ matrix of zeros and ones with ones on positions corresponding to I_{ij}. The covariance between $\tilde{T}_{t,ij}$ and $\tilde{T}_{t,i'j'}$ is $Cov(\tilde{T}_{t,ij}, \tilde{T}_{t,i'j'}) = \frac{1}{|I_{ij}|^2} e'_{ij} \Sigma_{\mathbf{X}} e_{i'j'}$. Thus, the elements of $\boldsymbol{\mu}$ and $\boldsymbol{G}$ can be uniquely determined from $\boldsymbol{\mu}_X$ and $\boldsymbol{\Sigma}_X$.

We wish to emphasize that in this work we do not assume that, for a fixed time point t, the variables $\tilde{T}_{t,ij}, i = 1, \ldots, r_1, j = 1, \ldots, r_2$ are spatially independent, as has been done in previously mentioned papers. Thus, the matrix $\boldsymbol{G}$ is not diagonal. Furthermore, we would like to emphasize how our work with the ROIs substantially reduces the dimensionality of the problem in question. For instance, if choosing non-overlapping sub-images of size $h_1 = h_2 = 100$, an original image containing 2000×2000 pixels reduces to 400 ROIs and $\mathbf{T}_t$ is a 400-dimensional vector. Thus, $\boldsymbol{T}_t$ is still a high-dimensional vector, but its dimension is dramatically smaller than that of the vector without sub-images which has $4 \cdot 10^6$ components. It is also worth noting that, in this paper, $\mathbf{T}_1, \mathbf{T}_2, \ldots$ are assumed to be independent random vectors. Note that this assumption is not fulfilled if the subject changes or moves over time, since the assumption of identically distributed random vectors is no longer fulfilled.

In this paper, we assume that the pixel intensities and the characteristics of ROIs follow a multivariate normal distribution. This restricts the choice of possible quantities of interest that we wish to control. For this reason, we have focused on monitoring the mean behavior of a sequence of independent multivariate normally distributed random vectors in our simulation study. Let $r = r_1 \cdot r_2$. Then, the change point model (3) can be rewritten as

$$\mathbf{T}_t \sim \begin{cases} \mathcal{N}_r(\boldsymbol{\mu}, \mathbf{G}), & t < \tau \\ \mathcal{N}_r(\boldsymbol{\mu} + \boldsymbol{\Delta}, \mathbf{G}), & t \geq \tau, \end{cases}, \quad t \geq 1, \tag{4}$$

where $\boldsymbol{\Delta} \neq \mathbf{0}$ and $\tau \in \mathbb{N} \cup \{\infty\}$. If $\tau = \infty$, we determine that the image process is in control and no change has happened. If $\tau < \infty$, then a shift had occured and the image process is out of control, starting from time point τ. Several control charts have been introduced in the literature to deal with the problem of how to monitor the mean behavior (cf. Section III). However, small dimensions have previously been assumed, e.g., values between 2 and 5. In the present case, the dimension is much higher! Furthermore, most of the charts that have been introduced have depended on certain design parameters (e.g., a smoothing matrix, a reference matrix, etc.) which must be determined in advance. This dramatically complicates the application of these methods in a high-dimensional case. For this reason, we prefer to work with a purely data-driven control scheme. For the change point model (4), we derive a generalized likelihood ratio chart (e.g., [36], [38], [39]) that will not depend on any additional design parameters.

Applying the generalized likelihood ratio procedure, we obtain the following control statistic at time point $n \geq 1$

$$R_n^* = \max_{1 \leq \eta \leq n} (n - \eta + 1) \hat{\boldsymbol{\Delta}}'_{\eta,n} \mathbf{G}^{-1} \hat{\boldsymbol{\Delta}}_{\eta,n}$$

with

$$\hat{\boldsymbol{\Delta}}_{\eta,n} = \frac{1}{n - \eta + 1} \sum_{t=\eta}^{n} \mathbf{T}_t - \boldsymbol{\mu}.$$

The detailed derivation is given in the appendix.

Sometimes, it is useful to standardize R_n^*. Since the moments of the maximum of non-independent variables are difficult to determine, we standardize by the moments of the statistic without taking the maximum into account, i.e., of $(n - \eta + 1) \hat{\boldsymbol{\Delta}}'_{\eta,n} \mathbf{G}^{-1} \hat{\boldsymbol{\Delta}}_{\eta,n}$. This procedure is useful for determining the control limits, as the control limits without standardization can be large and beyond the values of around 3 that are frequently employed in SPC. Note, however, that this form of standardization still does not guarantee that the distribution of the control statistic is independent of the covariance matrix $\mathbf{G}$. Since in the in-control case $\hat{\boldsymbol{\Delta}}_{\eta,n} \sim \mathcal{N}_r(\mathbf{0}, \frac{1}{n-\eta+1}\mathbf{G})$, it holds that $(n - \eta + 1) \hat{\boldsymbol{\Delta}}'_{\eta,n} \mathbf{G}^{-1} \hat{\boldsymbol{\Delta}}_{\eta,n} \sim \chi^2_r$, and, thus, its in-control expectation is r and its in-control variance is $2r$. The modified version of the statistic R_n^* looks as follows

$$R_n = \frac{\max_{1 \leq \eta \leq n} (n - \eta + 1) \hat{\boldsymbol{\Delta}}'_{\eta,n} \mathbf{G}^{-1} \hat{\boldsymbol{\Delta}}_{\eta,n} - r}{\sqrt{2r}}.$$

Now, the chart gives a signal at time $n \geq 1$ if $R_n > C_R$ with a suitable constant C_R, the so-called control limit.

In practice, $\boldsymbol{\mu}$ and $\mathbf{G}$ are both unknown and they have to be estimated by a prerun. Let us assume that a prerun of the observed process in the in-control state is given by $\mathcal{X} = (\mathbf{X}_{1-m}, \ldots, \mathbf{X}_0)'$. These values can be utilized to estimate $\boldsymbol{\mu}_X$ and $\boldsymbol{\Sigma}_X$, for example, employing the ML estimators

$$\hat{\boldsymbol{\mu}}_X = \frac{1}{m} \mathcal{X}' \mathbf{1}_m \text{ and } \hat{\boldsymbol{\Sigma}}_X = \frac{1}{m} (\mathcal{X}' (\boldsymbol{I}_m - \mathbf{1}_m \mathbf{1}'_m / m) \mathcal{X})$$

where $\mathbf{1}_m = (1, \ldots, 1)'$ is a vector of length m and $\boldsymbol{I}_m$ is the identity matrix of size $m \times m$. These values can be used to obtain estimators $\hat{\boldsymbol{\mu}}$ and $\hat{\boldsymbol{G}}$ for $\boldsymbol{T}_n$ as described at the beginning of this subsection.

Note that, to compute R_n, it is necessary to invert the $(r_1 \cdot r_2) \times (r_1 \cdot r_2)$ matrix $\mathbf{G}$ (or $\hat{\boldsymbol{G}}$). However, ML estimators will only provide suitable results if m is larger than $r_1 \cdots r_2$. In practice, this is usually not the case and, thus, the classical sample estimators fail in a high-dimensional context (e.g., [40]). The shrinkage approach (see [41]) provides another potential method of estimating the covariance matrix. This is a nonparametric estimator that works well even in a high-dimensional case. Thus, it can be applied in situations where the dimension $r_1 \cdot r_2$ is of moderate size with respect

to m. However, this approach will also fail if m is small. In such a case, a parametric or a semiparametric method seems to be more successful, though it is necessary to impose some assumptions on the structure of $\mathbf{G}$. Intuitively, it is reasonable to assume that more distant observations exhibit a weaker correlation than observations lying closer together. In this regard, we might even consider independence starting from a certain distance. It is also possible to make use of an isotropic covariance matrix with an exponential or a Matern covariance function (see [25]). In this case, the estimation of $\mathbf{G}$ is easier and much more robust, since only a few parameters need to be estimated. A further possibility, as has already been mentioned, is to assume a matrix-variate normal distribution in the form $\tilde{\mathbf{T}}_t \sim \mathcal{N}_{r_1,r_2}(\tilde{\boldsymbol{\mu}}, \mathbf{B}, \mathbf{C})$, where $\tilde{\boldsymbol{\mu}}$ is the matrix of mean values, $\mathbf{B}$ is the matrix which describes the covariances between the rows, and $\mathbf{C}$ is the matrix which describes the covariances between the columns of $\tilde{\mathbf{T}}_t$ (see [42]).

C. Modifications of the GLR Approach

A disadvantage of the control statistic obtained by the GLR approach is that it is necessary to determine the inverse matrix of $\mathbf{G}$. This is a computationally-demanding task for high dimensions. In fact, the control statistic R_n consists of a Mahalanobis distance. [40] and [43] consider a similar problem. Following [40], we replace the quantity $(n-\eta+1)\hat{\boldsymbol{\Delta}}'_{\eta,n}\mathbf{G}^{-1}\hat{\boldsymbol{\Delta}}_{\eta,n}$ with the quantity $(n-\eta+1)\hat{\boldsymbol{\Delta}}'_{\eta,n}\hat{\boldsymbol{\Delta}}_{\eta,n}-tr(\mathbf{G})$, which must be suitably normalized.

Lemma 1: Let $1 \leq \eta \leq n$. Then, in the in-control state, it holds that

$$E((n-\eta+1)\hat{\boldsymbol{\Delta}}'_{\eta,n}\hat{\boldsymbol{\Delta}}_{\eta,n}) = tr(\mathbf{G}),$$
$$Var((n-\eta+1)\hat{\boldsymbol{\Delta}}'_{\eta,n}\hat{\boldsymbol{\Delta}}_{\eta,n}) = 2\,tr(\mathbf{G}^2).$$

Proof: Without restriction, we suppose that $\boldsymbol{\mu} = \mathbf{0}$. We utilize the fact that $(\mathbf{T}_\eta, \ldots, \mathbf{T}_n) \overset{d}{=} (\mathbf{T}_1, \ldots, \mathbf{T}_{n-\eta+1})$. In order to simplify the notation, let $a = n-\eta+1$. Then

$$E(\frac{1}{a}\sum_{i,j=1}^{a}\mathbf{T}'_i\mathbf{T}_j) = \frac{1}{a}tr(E(\sum_{i,j=1}^{a}\mathbf{T}_i\mathbf{T}'_j)) = tr(\mathbf{G}),$$
$$Var(\frac{1}{a}\sum_{i,j=1}^{a}\mathbf{T}'_i\mathbf{T}_j) = \frac{1}{a^2}E(\sum_{i,j,\upsilon,l=1}^{a}\mathbf{T}'_i\mathbf{T}_j\mathbf{T}'_\upsilon\mathbf{T}_l) - (tr(\mathbf{G}))^2.$$

If there is one index which differs from the three others, then the expectation is 0. Thus, a non-zero contribution only results in the event that all indices are the same or if two pairs of indices are the same. If $i=j\neq\upsilon=l$, we get

$$E(\mathbf{T}'_i\mathbf{T}_j\mathbf{T}'_\upsilon\mathbf{T}_l) = E(\mathbf{T}'_i\mathbf{T}_i)E(\mathbf{T}'_\upsilon\mathbf{T}_\upsilon) = (tr(\mathbf{G}))^2$$

and this occurs $a(a-1)$ times. If $i=\upsilon\neq j=l$, we obtain

$$\begin{aligned}E(\mathbf{T}'_i\mathbf{T}_j\mathbf{T}'_\upsilon\mathbf{T}_l) &= E(\mathbf{T}'_i\mathbf{T}_j\mathbf{T}'_i\mathbf{T}_j) = E(\mathbf{T}'_j\mathbf{T}_i\mathbf{T}'_i\mathbf{T}_j)\\ &= tr(E(\mathbf{T}_i\mathbf{T}'_i\mathbf{T}_j\mathbf{T}'_j)) = tr(E(\mathbf{T}_i\mathbf{T}'_i)\\ &= E(\mathbf{T}_j\mathbf{T}'_j)) = tr(\mathbf{G}^2),\end{aligned}$$

and the number of times that this occurs is also the same. For $i=l\neq j=\upsilon$, it follows that

$$\begin{aligned}E(\mathbf{T}'_i\mathbf{T}_j\mathbf{T}'_\upsilon\mathbf{T}_l) &= E(\mathbf{T}'_i\mathbf{T}_j\mathbf{T}'_j\mathbf{T}_i)\\ &= tr(E(\mathbf{T}_j\mathbf{T}'_j\mathbf{T}_i\mathbf{T}'_i)) = tr(\mathbf{G}^2)\end{aligned}$$

and this can be observed $a(a-1)$ times.

Moreover, employing [44, 3.2b.10], we have

$$E(\mathbf{T}'_i\mathbf{T}_i\mathbf{T}'_i\mathbf{T}_i) = 2\,tr(\mathbf{G}^2) + (tr(\mathbf{G}))^2.$$

Thus, we get that

$$\begin{aligned}Var(\frac{1}{a}\sum_{i,j=1}^{a}\mathbf{T}'_i\mathbf{T}_j) &= \frac{a(2\,tr(\mathbf{G}^2)+(tr(\mathbf{G}))^2)}{a^2}\\ &\quad+\frac{a(a-1)(tr(\mathbf{G}))^2+2a(a-1)tr(\mathbf{G}^2)}{a^2}\\ &\quad-(tr(\mathbf{G}))^2\\ &= 2\,tr(\mathbf{G}^2).\end{aligned}$$

■

This leads to the new control statistic,

$$M_n = \frac{\max_{1\leq\eta\leq n}(n-\eta+1)\hat{\boldsymbol{\Delta}}'_{\eta,n}\hat{\boldsymbol{\Delta}}_{\eta,n} - tr(\mathbf{G})}{\sqrt{2\,tr(\mathbf{G}^2)}}.$$

The control chart signals whether the control statistic M_n exceeds some prespecified control limit C_M.

[43] provided an improvement of the approach of [40]. Applying their procedure in the present case, the control statistic is based on

$$\sum_{\substack{t,\upsilon=\eta,\\ t\neq\upsilon}}^{n}(\mathbf{T}_t-\boldsymbol{\mu})'(\mathbf{T}_\upsilon-\boldsymbol{\mu}).$$

Note that for $\eta=n$ the value of this statistic equals zero.

Lemma 2: Let $1 \leq \eta \leq n$. Then, in the in-control state, it holds that

$$E\left(\sum_{\substack{t,\upsilon=\eta,\\ t\neq\upsilon}}^{n}(\mathbf{T}_t-\boldsymbol{\mu})'(\mathbf{T}_\upsilon-\boldsymbol{\mu})\right) = 0,$$
$$\begin{aligned}&Var\left(\sum_{\substack{t,\upsilon=\eta,\\ t\neq\upsilon}}^{n}(\mathbf{T}_t-\boldsymbol{\mu})'(\mathbf{T}_\upsilon-\boldsymbol{\mu})\right)\\ &= 2(n-\eta+1)(n-\eta)\,tr(\mathbf{G}^2).\end{aligned}$$

Proof: Using the same argumentation as in the proof of the former lemma, we find that

$$\begin{aligned}&E\left(\left(\sum_{\substack{t,\upsilon=\eta,\\ t\neq\upsilon}}^{n}(\mathbf{T}_t-\boldsymbol{\mu})'(\mathbf{T}_\upsilon-\boldsymbol{\mu})\right)^2\right)\\ &= \sum_{\substack{t,\upsilon=\eta,\\ t\neq\upsilon}}^{n}\sum_{\substack{j,l=\eta,\\ j\neq l}}^{n}E\left((\mathbf{T}_t-\boldsymbol{\mu})'(\mathbf{T}_\upsilon-\boldsymbol{\mu})(\mathbf{T}_j-\boldsymbol{\mu})'(\mathbf{T}_l-\boldsymbol{\mu})\right).\end{aligned}$$

Now, we consider $E((\mathbf{T}_t-\boldsymbol{\mu})'(\mathbf{T}_v-\boldsymbol{\mu})(\mathbf{T}_j-\boldsymbol{\mu})'(\mathbf{T}_l-\boldsymbol{\mu}))$. If $t=j\neq v=l$ and $t=l\neq v=j$, then this expectation is equal to $tr(\mathbf{G}^2)$. This occurs $2(n-\eta+1)(n-\eta)$ times. In all other cases, the expectation is 0. Consequently,

$$E\left(\left(\sum_{\substack{t,v=\eta,\\ t\neq v}}^{n}(\mathbf{T}_t-\boldsymbol{\mu})'(\mathbf{T}_v-\boldsymbol{\mu})\right)^2\right) = 2(n-\eta+1)(n-\eta)tr(\mathbf{G}^2).$$

■

The attempt of [43] motivates the use of the control statistic $U_n=\max\{0,$

$$\max_{1\leq\eta\leq n-1}\frac{1}{\sqrt{2(n-\eta+1)(n-\eta)}}\frac{\sum_{\substack{t,v=\eta,\\ t\neq v}}^{n}(\mathbf{T}_t-\boldsymbol{\mu})'(\mathbf{T}_v-\boldsymbol{\mu})}{\sqrt{tr(\mathbf{G}^2)}}\}.$$

Note that in [40] and [43] the underlying statistics did not contain a maximum as they do in our case. Thus, the results of these authors cannot be applied to characterize the asymptotic distribution of our control statistics.

For calculating the control statistics M_n and U_n, only $O(r_1^2r_2^2)$ operations are necessary, while for the determination of R_n, an inverse matrix must be calculated, which is more time intensive. The Gauss-Jordan elimination method requires $O(r_1^3r_2^3)$ operations. Thus, these quantities can be determined more qucikly and, consequently, they can be applied to smaller sizes of ROIs and, therefore, to more ROIs.

A control chart gives a signal if the corresponding control statistic exceeds a control limit, for example, $U_n > C_U$. The run length of the chart, i.e., the number of periods until a signal, is then defined as

$$RL_U(C_U)=inf\{n\in\mathbb{N}\mid U_n>C_U\}.$$

The control limits are determined such that, in the in-control state, the expectation or the median of the run length (ARL or MRL, respectively) attains a prespecified value ξ. However, the ARL is not a suitable choice if the distribution of the run length is skewed or heavy-tailed. For this reason, we consider the MRL which is robust against these features. The control limit C_U solves the equation

$$\text{Median}(RL_U(C_U))=\xi.$$

We determine the control limits for the remaining two charts similarly.

IV. Simulation Study

In order to compare the charts that are introduced, we consider the in-control process to be a computer-generated image that represents a primitive sketch of a front page of a book or of a magazine, such as in Fig. 1. This figure defines the nominal image in our study. The intensities of the pixels of the further generated images are defined by the values of $f_{ij}+a_{ij}$, as in equations (2) and (3). We set the size of every image to 300×180 pixels and every image consists of sub-images that represent different parts of the front page, with different color patterns. For example, a very dark stripe at the top of

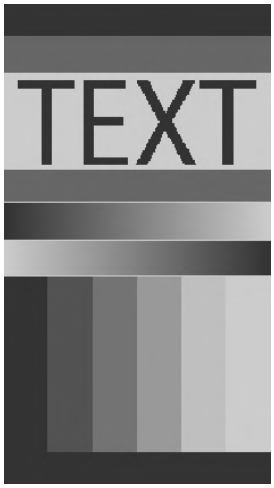

Fig. 1. A computer-generated image (the actual size is 300×180 pixels).

the image in Fig. 1 consists of 3,420 (19×180) pixels and all of these pixels in this part of the image have the same mean intensity value $f_{ij}=0.2$. The dynamic intensities $\tilde{X}_{t,ij}, i=1,\ldots,300,\ j=1,\ldots,180$ of every pixel are assumed to follow a normal distribution with parameters f_{ij} and σ_{ij}^2. Thus, the in-control mean values of the pixels are set as equal to the intensity values of the nominal image. All in-control variances $\sigma_{ij}^2, i=1,\ldots,300,\ j=1,\ldots,180$ equal 0.03^2. Small variances and f_{ij} within the interval $[0.2; 0.8]$ guarantee that the intensities simulated with these parameters stay within the unit interval. We introduce the spatial correlation of the pixel intensities by exploiting the Euclidean distance between the pixels and the exponential transformation. More precisely, $Corr(\tilde{X}_{t,ij},\tilde{X}_{t,i'j'})=Corr(e_{t,ij},e_{t,i'j'})=0.9^{\sqrt{(i'-i)^2+(j'-j)^2}}$ for $i,i'=1,\ldots,300,\ j,j'=1,\ldots,180$ in the in-control situation. The constant, 0.9, was chosen due to the aforementioned remark that neighboring pixels have a strong positive spatial correlation.

We consider three different settings for the choice of ROIs:

a) ROIs of the size 10×10 pixels, resulting in 540 non-overlapping ROIs (schematically shown in Fig. 2, top);

b) ROIs of the size 20×20 pixels, resulting in 135 non-overlapping ROIs (schematically shown in Fig. 2, bottom);

c) ROIs of the size 20×20 pixels, resulting in 493 overlapping ROIs (the behavior of the overlapping ROIs is sketched in Fig. 3).

To distinguish between these three settings for the charts based on the R control statistics, we employ superscripts, for example, $R^{(10)}$, $R^{(20)}$, and $R^{(20ov)}$. The analysis can be extended to other types of ROIs either of fixed or varying sizes.

For every setting, we derive the mean and the covariance matrix of the local mean $\tilde{T}_{t,ij}$ relying on the distributional assumptions of the pixel intensities mentioned previously. Next, without losing generality and to ease the computational load, we simulate the values of $\tilde{T}_{t,ij}$ rather than the intensity values $\tilde{X}_{t,ij}$ of the pixels. Note that the exact distribution of the control statistics R_n, M_n, and U_n introduced in the previous chapters is not a standard distribution. For that reason,

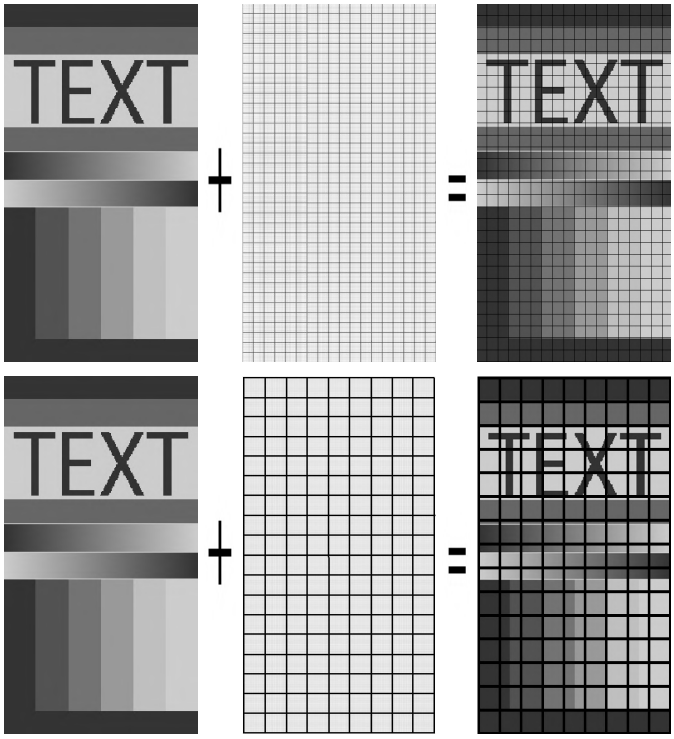

Fig. 2. Top: Partitioning of the 300×180 pixel image in 10×10 ROIs. Bottom: Partitioning of the 300×180 pixel image in 20×20 ROIs.

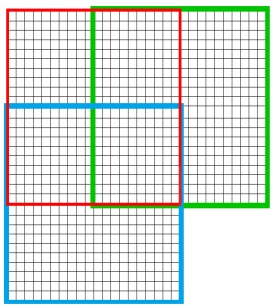

Fig. 3. Sketch of the overlapping for the 20×20 ROIs.

the control limits of the control charts are calculated using simulations. As a calibration criterion, we set the in-control median run length (MRL_0) to equal $\xi = 100$. To verify the robustness of the suggested monitoring technique for the choice of ξ, we repeat the completed analysis for $\xi = 200$. The results and the conclusions were almost identical to the findings for $\xi = 100$; therefore, we will past them to save space.

In practice, the nonlinear equation $\text{Median}(RL(C)) - \xi = 0$ for the control limit C is solved numerically. Here, we utilize a adapted version of the *bisection* method, since this technique does not require derivatives of the underlying function. For each iteration of the bisection algorithm we estimate the median using $25,000$ independent runs, i.e., $25,000$ times we run the control chart with simulated data until there is a signal, collecting data on the observed run lengths. The resulting control limits are provided in Table I.

A guide for a practitioner on how to estimate the control limit could consist of the next steps:

TABLE I

CONTROL LIMITS CALIBRATED TO ATTAIN THE MEDIAN IN-CONTROL RUN LENGTH OF $\xi = 100$

$C_{R(10)}$	$C_{R(20)}$	$C_{R(20ov)}$	$C_{M(10)}$	$C_{M(20)}$	$C_{M(20ov)}$	$C_{U(10)}$	$C_{U(20)}$	$C_{U(20ov)}$
3.178	3.328	3.185	3.475	3.548	3.598	3.283	3.331	3.36

a) Choose two starting values $A_1, A_2 \in \mathbb{R}$ in a way that $\text{Median}(RL(A_1)) - \xi < 0$ and $\text{Median}(RL(A_2)) - \xi > 0$ with a small number of replications (for example, $400 - 500$). Keep in mind that the number or replications could be different in another type of the in-control settings (i.e., different size of the image, size of the ROI, etc.);

b) Check the sign of $\text{Median}(RL(\frac{A_1+A_2}{2})) - \xi$. If it is > 0, put $A_2 := \frac{A_1+A_2}{2}$, otherwise put $A_1 := \frac{A_1+A_2}{2}$;

c) Keep performing the step b) till $\text{Median}(RL(\frac{A_1+A_2}{2})) - \xi$ equals to one of the next values $-5, -4, -3, \ldots, 4, 5$. Simultaneously, increase the number of replications (for example, to $3000 - 5000$) to obtain a more precise result;

d) If the computed $\text{Median}(RL(\frac{A_1+A_2}{2}))$ equals $\xi \pm 2$ for the chosen number of replications, then adopt $\frac{A_1+A_2}{2}$ as the control limit.

To check the ability of the charts to signal in the out-of-control state, we consider the following five scenarios for a change in the mean value of the image areas:

a) The second horizontal stripe, sized 23×180 pixels, becomes brighter. All pixels in this stripe are fully covered by 72 non-overlapping ROIs of the size 10×10 pixels. The mean value of the affected pixels changes from $f_{ij} = 0.4$, $i = 1, \ldots 300$, $j = 1, \ldots 180$ to $f_{ij} + \delta$ with $\delta \in \{0.005, 0.01, \ldots, 0.05\}$. Fig. 4 contains the image with $\delta = 0.15$ in its upper middle part. Based on a purely visual inspection, this shift is the only one that can be identified clearly, while the identification of smaller shifts is hardly possible. In Fig. 5, the histogram of the distribution of the out-of-control RL for the shift $\delta = 0.02$ is plotted to give the reader a feeling how long it could take before the chart detected this change. The histogram demonstrates that less than 23 observations would be required.

b) The background area of the word "TEXT" in the computer-generated image, sized 61×180 pixels, becomes darker. The mean value of those pixels is 0.8. The values for the intensity shifts in the mean are $\delta \in \{-0.005, -0.01, \ldots, -0.05\}$.

c) The word "TEXT" (in which all $2,550$ pixel intensities equal 0.2) becomes brighter. The intensity values are shifted by $\delta \in \{0.005, 0.01, \ldots, 0.05\}$.

d) The fourth horizontal stripe in the image, sized 23×180 pixels, becomes darker. The intensity values are shifted by $\delta \in \{-0.005, -0.01, \ldots, -0.05\}$. Compared with scenario 1, all pixels in this stripe are fully covered by 54 non-overlapping ROIs of the size 10×10 pixels.

e) The left half of the image gets darker. The intensity values are shifted by $\delta \in \{-0.005, -0.01, \ldots, -0.025\}$.

Fig. 4 illustrates the changes in scenarios a) – e). These images visualize the shifted mean intensities $f_{ij} + a_{ij}$ without the noise component. The corresponding out-of-control MRLs,

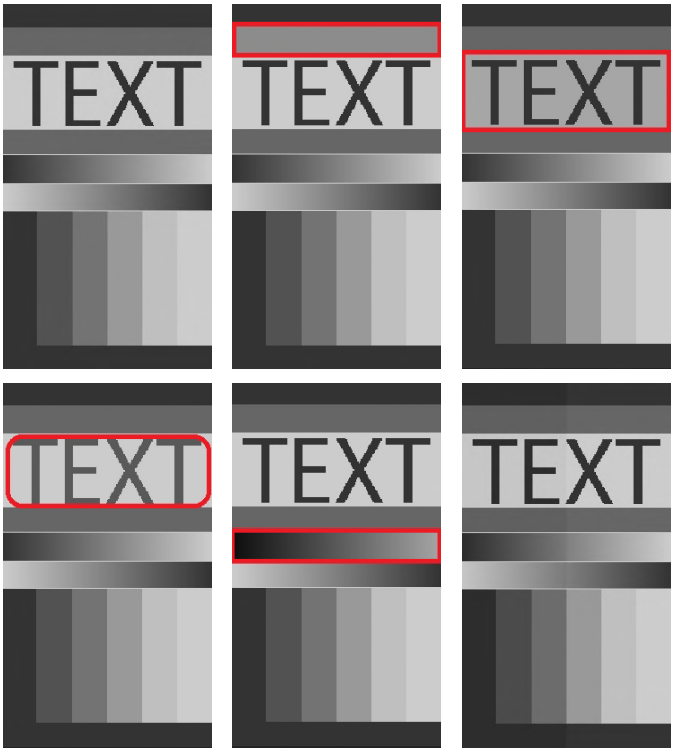

Fig. 4. The computer-generated images. Top: left – without change; middle – change, type a); right – change, type b). Bottom: left – change, type c); middle – change, type d); right – change, type e). The shifts are $\delta = 0.15$ for changes a) — d) and $\delta = 0.025$ for change e).

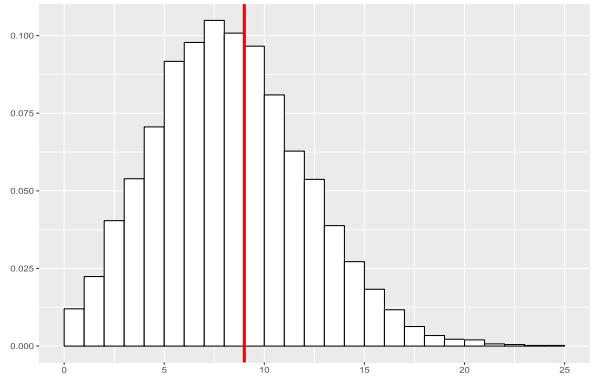

Fig. 5. Histogram of the out-of-control RL for the R_n^{10} chart. Case a), $\delta = 0.02$, 10^4 repetitions. The red line indicates the corresponding out-of-control MRL.

TABLE II

OUT-OF-CONTROL MRLS OF THE CONTROL CHARTS R_n, M_n, AND U_n FOR THE SCENARIOS DESCRIBED IN A) – E)

	shift, δ									
	0.005	0.01	0.015	0.02	0.025	0.03	0.035	0.04	0.045	0.05
Change, type a)										
$R_n^{(10)}$	65	28	15	9	6	4	3	2	2	1
$R_n^{(20)}$	51	19	9	6	4	2	2	1	1	1
$R_n^{(20ov)}$	64	28	14	8	5	4	3	2	2	1
$M_n^{(10)}$	54	21	11	6	4	3	2	2	1	1
$M_n^{(20)}$	52	20	10	6	4	3	2	1	1	1
$M_n^{(20ov)}$	56	23	12	7	4	3	2	2	1	1
$U_n^{(10)}$	51	20	10	5	3	2	1	1	1	1
$U_n^{(20)}$	49	18	9	5	3	2	1	1	1	1
$U_n^{(20ov)}$	53	21	10	6	4	2	2	1	1	1
Change, type b)										
$R_n^{(10)}$	49	19	9	5	3	2	2	1	1	1
$R_n^{(20)}$	49	19	9	5	3	2	2	1	1	1
$R_n^{(20ov)}$	51	19	9	5	3	2	2	1	1	1
$M_n^{(10)}$	38	13	6	4	2	2	1	1	1	1
$M_n^{(20)}$	37	13	6	3	2	1	1	1	1	1
$M_n^{(20ov)}$	38	13	6	4	2	2	1	1	1	1
$U_n^{(10)}$	35	12	5	3	2	1	1	1	1	1
$U_n^{(20)}$	33	11	5	3	2	1	1	1	1	1
$U_n^{(20ov)}$	35	12	6	3	2	1	1	1	1	1
Change, type c)										
$R_n^{(10)}$	64	29	15	9	6	4	3	2	2	1
$R_n^{(20)}$	83	51	30	19	13	9	7	5	4	4
$R_n^{(20ov)}$	66	30	16	9	6	4	3	2	2	1
$M_n^{(10)}$	82	48	28	18	12	9	6	5	4	3
$M_n^{(20)}$	84	52	32	20	14	10	8	6	5	4
$M_n^{(20ov)}$	83	52	32	21	15	11	8	6	5	4
$U_n^{(10)}$	78	45	26	16	11	8	6	4	3	3
$U_n^{(20)}$	81	48	29	19	13	9	7	5	4	3
$U_n^{(20ov)}$	80	49	30	19	13	9	7	5	4	3
Change, type d)										
$R_n^{(10)}$	71	35	19	11	7	5	4	3	2	2
$R_n^{(20)}$	65	29	15	9	6	4	3	2	2	1
$R_n^{(20ov)}$	70	35	18	11	7	5	4	3	2	2
$M_n^{(10)}$	56	23	12	7	5	3	2	2	1	1
$M_n^{(20)}$	60	24	13	8	5	3	2	2	1	1
$M_n^{(20ov)}$	57	24	12	7	5	3	2	2	1	1
$U_n^{(10)}$	53	21	10	6	4	2	2	1	1	1
$U_n^{(20)}$	56	22	11	6	4	3	2	1	1	1
$U_n^{(20ov)}$	53	22	11	6	4	3	2	1	1	1
Change, type e)										
$R_n^{(10)}$	31	10	4	2	1	—	—	—	—	—
$R_n^{(20)}$	24	7	3	2	1	—	—	—	—	—
$R_n^{(20ov)}$	31	10	4	2	1	—	—	—	—	—
$M_n^{(10)}$	12	3	1	1	1	—	—	—	—	—
$M_n^{(20)}$	12	3	1	1	1	—	—	—	—	—
$M_n^{(20ov)}$	12	3	2	1	1	—	—	—	—	—
$U_n^{(10)}$	11	3	1	1	1	—	—	—	—	—
$U_n^{(20)}$	11	3	1	1	1	—	—	—	—	—
$U_n^{(20ov)}$	11	3	1	1	1	—	—	—	—	—

based on the 10^4 repetitions, can be found in Table II and Fig. 6. The charts are then calibrated to attain the $\text{MRL}_0 = 100$ in the in-control state; therefore, all curves start at $(0, 100)$. The MRLs rapidly decrease for most types of changes and the MRL of 20 is attained for the shift $\delta = 0.01$. Note that a change in intensity by 0.01 is, in fact, almost invisible to the human eye, yet the chart manages to detect the change quickly after the shift occurs.

While none of the charts have shown the best performance in all scenarios, U_n with the non-overlapping ROIs of the size 20×20 pixels has delivered the best results in three out of five of the out-of-control scenarios. In the third out-of-control scenario, the R_n chart appears to be the best. In the third scenario, the smallest number of pixels were changed when compared with the others, which could be a possible reason for the better performance of the R_n chart in this case. The disadvantage of R_n is that, contrary to M_n and U_n, it depends on the inverse of the covariance matrix. This quantity is difficult to determine in a high-dimensional situation. Moreover, in this paper, we do not discuss the influence of parameter estimation on the charts; the determination of the inverse would be even more complicated taking into account the estimation risk.

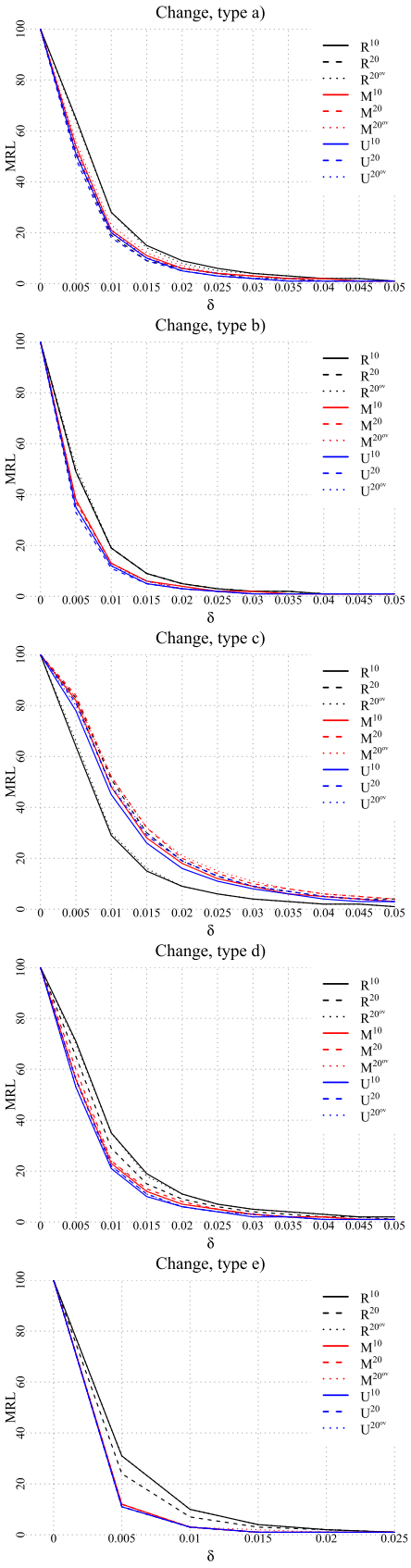

Fig. 6. Out-of-control MRLs of the control charts R_n, M_n, and U_n for the scenarios described in a) – e).

To assess the advantages of the proposed monitoring schemes, we choose the Hotelling's T^2 multivariate control chart as a benchmark. We again assume that the mean vector and the covariance matrix are known, to guarantee a fair comparison. The standardized version of the control statistic at time n is given by

$$T_n^2 = \frac{(\mathbf{T}_n - \boldsymbol{\mu})' \boldsymbol{G}^{-1} (\mathbf{T}_n - \boldsymbol{\mu}) - r}{\sqrt{2r}}.$$

Note that, in the in-control case, the non-standardized control statistic follows a χ^2-square distribution with r degrees of freedom, where r is the dimension of the vector $\mathbf{T}_i$. Since we employ the MRL as the performance measure, we cannot utilize our knowledge of the distribution of the control statistic T_n^2 to determine the control limits and, thereby, determine them numerically as above. The control limits for the chosen sizes of the ROIs $C_{H^{(10)}}, C_{H^{(20)}}, C_{H^{(20ov)}}$ with $\text{MRL}_0 = 100$ are estimated using 25,000 independent repetitions; they can be found in Table III. The out-of-control MRLs for the scenarios a) — e) are given in Table IV. According to the out-of-control MRLs, our new charts perform better than the Hotelling's T^2 in general.

Intuitively, the ability of the charts to signal (whether the control limit has been exceeded) depends on the choice of the minimal size of the ROI. As is analyzed in [35], the size of the ROI should be chosen similar to the size of the area of the expected defect. If the size of the ROI is smaller than the expected area of the defect, then the chart would supposedly signal faster than in the case where the size of the ROI is larger.

TABLE III

CONTROL LIMITS OF THE HOTELLING'S T_n^2 CHART WITH THE MEDIAN IN-CONTROL RUN LENGTH OF $\xi = 100$

$C_{H^{(10)}}$	$C_{H^{(20)}}$	$C_{H^{(20ov)}}$
2.562	2.663	2.565

TABLE IV

OUT-OF-CONTROL MRLS OF THE HOTELLING'S T_n^2 CHART FOR THE SCENARIOS A) – E)

	shift, δ									
	0.005	0.01	0.015	0.02	0.025	0.03	0.035	0.04	0.045	0.05
Change, type a)										
$H_n^{(10)}$	94	81	63	43	29	19	11	7	4	3
$H_n^{(20)}$	91	70	45	26	15	8	4	3	2	1
$H_n^{(20ov)}$	94	79	59	42	27	17	10	6	4	3
Change, type b)										
$H_n^{(10)}$	90	69	46	26	14	8	4	2	2	1
$H_n^{(20)}$	91	68	43	25	13	7	4	2	2	1
$H_n^{(20ov)}$	90	70	45	27	15	8	4	2	2	1
Change, type c)										
$H_n^{(10)}$	95	81	63	45.5	30	19	12	7	5	3
$H_n^{(20)}$	97	93	81	70	56	45	35	26	19	14
$H_n^{(20ov)}$	95	81	66	47	32	20	13	8	5	3
Change, type d)										
$H_n^{(10)}$	94	86	71	53	39	27	18	12	8	5
$H_n^{(20)}$	94	82	60	43	29	18	12	7	4	3
$H_n^{(20ov)}$	95	84	67	53	38	26	18	11	7	5
Change, type e)										
$H_n^{(10)}$	84	49	22	9	3	–	–	–	–	–
$H_n^{(20)}$	76	35	13	4	2	–	–	–	–	–
$H_n^{(20ov)}$	81	49	21	9	4	–	–	–	–	–

TABLE V
OUT-OF-CONTROL MRLS, MEANS AND STANDARD DEVIATIONS FOR THE $R^{(20)}$ CHART IN SCENARIO A)

	shift, δ									
	0.005	0.01	0.015	0.02	0.025	0.03	0.035	0.04	0.045	0.05
	$R_n^{(20)}$									
MRL	51	19	9	6	4	2	2	1	1	1
Mean	57.595	20.157	9.884	5.821	3.705	2.566	1.824	1.400	1.163	1.048
Std.Dev.	37.318	10.174	4.506	2.542	1.637	1.123	0.797	0.568	0.384	0.214

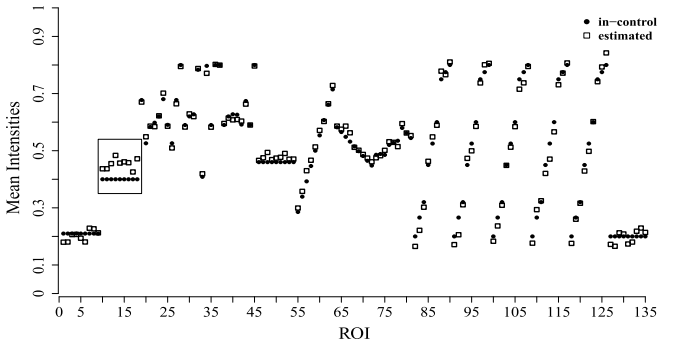

Fig. 7. Indexed ROIs and the corresponding in-control and estimated mean intensities for the $R^{(20)}$ chart in scenario a), $\delta = 0.05$, shifts are in ROIs 10–18.

We believe that a similar statement could be made concerning the number of changed pixels when the changes in the area are no longer convex, as in the third scenario. The advantage of overlapping ROIs is also seen in the third scenario, in which the chart with overlapping ROIs sized 20×20 pixels performed better than its non-overlapping same-sized counterpart.

There are many additional methods that benefit a practitioner when employing monitoring techniques with image data. Some of these are typical for monitoring in general, i.e., change point detection, while others are more specific, since they are used only for monitoring image processes. We demonstrate some of these methods, applying the performance of the control chart $R^{(20)}$ in the first out-of-control situation a).

To gain more information about the distribution of the run lengths, one could also compute its mean and standard deviation in addition to its median, as in Table V. As can be seen in the table, we find that for larger shifts the mean and the median are similar while using $R^{(20)}$. The values of the standard deviation, meanwhile, are large for small shifts and become smaller with larger δ.

After the chart signals, an additional plot can be generated, as in Fig. 7, to estimate the size of the shift in the mean intensities of the ROIs. To this end, we ordered the ROIs from left to right and, top to bottom, utilizing the partitioning in the bottom of Fig. 2, and plotted their index on the horizontal axis. The corresponding mean intensities were plotted on the vertical axis. Black circles illustrate the in-control mean intensities, while transparent squares indicate the estimated mean intensities after the signal. In scenario a), the faulty area is mostly covered by the ROIs $10-18$ and the large resulting changes can be seen in the plot.

Reference [35] advise that the Dice similarity coefficient (DSC) could be employed to determine how well a chart estimates the size of the change. Since we use ROIs of a fixed size, we compute the DSC as an assessment tool to associate the ROIs and the area where the shift occurred. Let F denote the area of the change. Then the DSC for the ith ROI is defined as

$$DSC_i = \frac{2|F \cap I_i|}{|F| + |I_i|}.$$

In our setting, we focus on the maximum of DSC_i's, i.e., the $DSC_{max} = \max_i \ DSC_i$, and, thus, the largest fraction of the fault area covered by a single ROI. DSC equal to one implies that the fault area is completely covered by a single ROI. Small values of DSC_i indicate that the ith ROI covers only a small fraction of the faulty area. For the statistic $R^{(20)}$ and scenario a), the maximal possible $DSC_{max} = \frac{2\times(20\times20)}{23\times180+20\times20} = \frac{40}{227} \approx 0.176$. This motivates further research on the optimal or dynamical choice of ROIs.

V. CONCLUSION

In this paper, we have discussed the problem of monitoring an image process over time. Since the number of pixels is huge, we face a high-dimensional problem and, for that reason, methods for high-dimensional data should be applied in particular. While many authors assume an independent residual process, we have taken the spatial correlation structure of the pixels into account. In order to reduce the dimensionality of the data, we built ROIs for every image and utilized the local statistical characteristics of those ROIs. We considered three possible control statistics and motivated them. In an extensive simulation study, we compare these three control designs with each other in various out-of-control situations. The chart U_n demonstrated results that were moderately better than those for the other two charts. The two control charts, M_n and U_n, employ simpler control statistics that are much easier to handle in a high-dimensional setting than R_n.

APPENDIX
DERIVATION OF THE GLR CHART

Proof: Assuming a change at position $1 \le \eta \le n$, the density of $\mathbf{T}_1, \dots \mathbf{T}_n$ is given by

$$f_\eta(\mathbf{T}_1, \dots, \mathbf{T}_n) = \frac{1}{(2\pi)^{\frac{rn}{2}} (\det \mathbf{G})^{\frac{n}{2}}} \times \exp\left(-\frac{1}{2} \sum_{t=1}^{\eta-1} (\mathbf{T}_t - \boldsymbol{\mu})' \mathbf{G}^{-1} (\mathbf{T}_t - \boldsymbol{\mu}) - \frac{1}{2} \sum_{t=\eta}^{n} (\mathbf{T}_t - \boldsymbol{\mu} - \boldsymbol{\Delta})' \mathbf{G}^{-1} (\mathbf{T}_t - \boldsymbol{\mu} - \boldsymbol{\Delta}) \right).$$

Thus,

$$-2 \log f_\eta(\mathbf{T}_1, \dots, \mathbf{T}_n) = 2 \log((2\pi)^{\frac{rn}{2}} (\det \mathbf{G})^{\frac{n}{2}}) + \sum_{t=1}^{\eta-1} (\mathbf{T}_t - \boldsymbol{\mu})' \mathbf{G}^{-1} (\mathbf{T}_t - \boldsymbol{\mu}) + \sum_{t=\eta}^{n} (\mathbf{T}_t - \boldsymbol{\mu} - \boldsymbol{\Delta})' \mathbf{G}^{-1} (\mathbf{T}_t - \boldsymbol{\mu} - \boldsymbol{\Delta}).$$

Setting

$$\frac{\delta}{\delta \boldsymbol{\Delta}}(-2\log f_\eta(\mathbf{T}_1,\ldots,\mathbf{T}_n)) = 2(n-\eta+1)\mathbf{G}^{-1}\boldsymbol{\Delta} - 2\sum_{t=\eta}^{n}\mathbf{G}^{-1}(\mathbf{T}_t-\boldsymbol{\mu}) = 0$$

leads to

$$\hat{\boldsymbol{\Delta}}_{\eta,n} = \frac{1}{n-\eta+1}\sum_{t=\eta}^{n}(\mathbf{T}_t-\boldsymbol{\mu}) = \frac{1}{n-\eta+1}\sum_{t=\eta}^{n}\mathbf{T}_t - \boldsymbol{\mu}.$$

Let f_0 denote the density of f under the null hypothesis, e.g., $H_0 : \boldsymbol{\Delta} = \mathbf{0}$. Consequently,

$$\begin{aligned}
&-2\log f_0(\mathbf{T}_1,\ldots,\mathbf{T}_n) + 2\log \max_{0\le\eta\le n}\max_{\boldsymbol{\Delta}} f_\eta(\mathbf{T}_1\ldots,\mathbf{T}_n)\\
&= \max\left\{0, \max_{1\le\eta\le n}\left(\sum_{t=\eta}^{n}(\mathbf{T}_t-\boldsymbol{\mu})'\mathbf{G}^{-1}(\mathbf{T}_t-\boldsymbol{\mu})\right)\right.\\
&\quad\left. - \sum_{t=\eta}^{n}(\mathbf{T}_t-\boldsymbol{\mu}-\hat{\boldsymbol{\Delta}}_{\eta,n})'\mathbf{G}^{-1}(\mathbf{T}_t-\boldsymbol{\mu}-\hat{\boldsymbol{\Delta}}_{\eta,n})\right\}\\
&= \max\left\{0, \max_{1\le\eta\le n}\left(2\hat{\boldsymbol{\Delta}}'_{\eta,n}\mathbf{G}^{-1}\sum_{t=\eta}^{n}(\mathbf{T}_t-\boldsymbol{\mu})\right.\right.\\
&\quad\left.\left. - (n-\eta+1)\hat{\boldsymbol{\Delta}}'_{\eta,n}\mathbf{G}^{-1}\hat{\boldsymbol{\Delta}}_{\eta,n}\right)\right\}\\
&= \max_{1\le\eta\le n}(n-\eta+1)\hat{\boldsymbol{\Delta}}'_{\eta,n}\mathbf{G}^{-1}\hat{\boldsymbol{\Delta}}_{\eta,n}.
\end{aligned}$$

Thus, the control statistic is given by

$$R_n = \max_{1\le\eta\le n}(n-\eta+1)\hat{\boldsymbol{\Delta}}'_{\eta,n}\mathbf{G}^{-1}\hat{\boldsymbol{\Delta}}_{\eta,n}.$$

■

REFERENCES

[1] R. C. Gonzalez and R. E. Woods, *Digital Image Processing*. Upper Saddle River, NJ, USA: Prentice-Hall, 2018.

[2] P. Fieguth, *Statistical Image Processing and Multidimensional Modeling*. New York, NY, USA: Springer, 2010.

[3] B. M. Colosimo, "Modeling and monitoring methods for spatial and image data," *Qual. Eng.*, vol. 30, no. 1, pp. 94–111, Jan. 2018.

[4] F. M. Megahed, W. H. Woodall, and J. A. Camelio, "A review and perspective on control charting with image data," *J. Qual. Technol.*, vol. 43, no. 2, pp. 83–98, Apr. 2011.

[5] R. L. Horst and M. Negin, "Vision system for high-resolution dimensional measurements and on-line SPC: Web process application," *IEEE Trans. Ind. Appl.*, vol. 28, no. 4, pp. 993–997, 1992.

[6] J. M. Armingol, J. Otamendi, A. De La Escalera, J. M. Pastor, and F. J. Rodriguez, "Statistical pattern modeling in vision-based quality control systems," *J. Intell. Robot. Syst.*, vol. 37, no. 3, pp. 321–336, 2003.

[7] H. B. Nembhard, N. J. Ferrier, T. A. Osswald, and J. R. Sanz-Uribe, "An integrated model for statistical and vision monitoring in manufacturing transitions," *Qual. Rel. Eng. Int.*, vol. 19, no. 6, pp. 461–476, 2003.

[8] R. L. Mason, N. D. Tracy, and J. C. Young, "A practical approach for interpreting multivariate t2 control chart signals," *J. Qual. Technol.*, vol. 29, no. 4, pp. 396–406, Oct. 1997.

[9] L.-I. Tong, C.-H. Wang, and C.-L. Huang, "Monitoring defects in IC fabrication using a hotelling T^2 control chart," *IEEE Trans. Semicond. Manuf.*, vol. 18, no. 1, pp. 140–147, Feb. 2005.

[10] J. J. Liu and J. F. MacGregor, "Estimation and monitoring of product aesthetics: Application to manufacturing of 'engineered stone countertops,"' *Mach. Vis. Appl.*, vol. 16, no. 6, p. 374, 2006.

[11] H.-D. Lin, "Automated visual inspection of ripple defects using wavelet characteristic based multivariate statistical approach," *Image Vis. Comput.*, vol. 25, no. 11, pp. 1785–1801, Nov. 2007.

[12] H.-D. Lin, "Computer-aided visual inspection of surface defects in ceramic capacitor chips," *J. Mater. Process. Technol.*, vol. 189, nos. 1–3, pp. 19–25, Jul. 2007.

[13] H.-D. Lin, C.-Y. Chung, and W.-T. Lin, "Principal component analysis based on wavelet characteristics applied to automated surface defect inspection," *WSEAS Trans. Comput. Res.*, vol. 3, no. 4, pp. 193–202, 2008.

[14] B. C. Jiang, C.-C. Wang, and H.-C. Liu, "Liquid crystal display surface uniformity defect inspection using analysis of variance and exponentially weighted moving average techniques," *Int. J. Prod. Res.*, vol. 43, no. 1, pp. 67–80, Jan. 2005.

[15] C.-J. Lu and D.-M. Tsai, "Automatic defect inspection for LCDs using singular value decomposition," *Int. J. Adv. Manuf. Technol.*, vol. 25, nos. 1–2, pp. 53–61, Jan. 2005.

[16] M. Koosha, R. Noorossana, and F. Megahed, "Statistical process monitoring via image data using wavelets," *Qual. Rel. Eng. Int.*, vol. 33, no. 8, pp. 2059–2073, Dec. 2017.

[17] E. Rafajłowicz and W. Rafajłowicz, "Image-driven decision making with application to control gas burners," in *Proc. IFIP Int. Conf. Comput. Inf. Syst. Ind. Manage.* Cham, Switzerland: Springer, 2017, pp. 436–446.

[18] Y. Lyu, J. Chen, Junghui and Z. Song, "Image-based process monitoring using deep learning framework," *Chemometrics Intell. Lab. Syst.*, vol. 189, pp. 8–17, Jun. 2019.

[19] M. Grasso, A. G. Demir, B. Previtali, and B. M. Colosimo, "*In situ* monitoring of selective laser melting of zinc powder via infrared imaging of the process plume," *Robot. Comput.-Integr. Manuf.*, vol. 49, pp. 229–239, Feb. 2018.

[20] M. Grasso and B. M. Colosimo, "A statistical learning method for image-based monitoring of the plume signature in laser powder bed fusion," *Robot. Comput.-Integr. Manuf.*, vol. 57, pp. 103–115, Jun. 2019.

[21] K. He, Q. Zhang, and Y. Hong, "Profile monitoring based quality control method for fused deposition modeling process," *J. Intell. Manuf.*, vol. 30, no. 2, pp. 947–958, Feb. 2019.

[22] T. Huang, S. Wang, S. Yang, and W. Dai, "Statistical process monitoring in a specified period for the image data of fused deposition modeling parts with consistent layers," *J. Intell. Manuf.*, pp. 1–16, Jul. 2020.

[23] P. Réfrégier and F. Goudail, *Statistical Image Processing Techniques for Noisy Images: An Application-Oriented Approach*. New York, NY, USA: Springer, 2013.

[24] M. Sonka, V. Hlavac, and R. Boyle, *Image Processing, Analysis, and Machine Vision*. Boston, MA, USA: Cengage Learning, 2014.

[25] N. Cressie and C. K. Wikle, *Statistics for Spatio-Temporal Data*. Hoboken, NJ, USA: Wiley, 2015.

[26] D. C. Montgomery, *Statistical Quality Control*. New York, NY, USA: Wiley, 2009.

[27] H. Hotelling, "Multivariate quality control illustrated by the air testing of sample bombsights," in *Techniques of Statistical Analysis*. New York, NY, USA: McGraw-Hill, 1947.

[28] C. A. Lowry, W. H. Woodall, C. W. Champ, and S. E. Rigdon, "A multivariate exponentially weighted moving average control chart," *Technometrics*, vol. 34, no. 1, pp. 46–53, 1992.

[29] R. S. Sparks, "Quality control with multivariate data," *Austral. J. Statist.*, vol. 34, no. 3, pp. 375–390, Sep. 1992.

[30] A. Fassó, "One-sided MEWMA control charts," *Commun. Statist.-Simul. Comput.*, vol. 28, no. 2, pp. 381–401, 1999.

[31] D. M. Hawkins, S. Choi, and S. Lee, "A general multivariate exponentially weighted moving-average control chart," *J. Qual. Technol.*, vol. 39, no. 2, pp. 118–125, Apr. 2007.

[32] J. D. Healy, "A note on multivariate CUSUM procedures," *Technometrics*, vol. 29, no. 4, pp. 409–412, Nov. 1987.

[33] R. B. Crosier, "Multivariate generalizations of cumulative sum quality-control schemes," *Technometrics*, vol. 30, no. 3, pp. 291–303, Aug. 1988.

[34] J. J. Pignatiello, Jr., and G. C. Runger, "Comparisons of multivariate CUSUM charts," *J. Qual. Technol.*, vol. 22, pp. 173–186, Jul. 1990.

[35] F. M. Megahed, L. J. Wells, J. A. Camelio, and W. H. Woodall, "A spatiotemporal method for the monitoring of image data," *Qual. Rel. Eng. Int.*, vol. 28, no. 8, pp. 967–980, Dec. 2012.

[36] Z. He, L. Zuo, M. Zhang, and F. M. Megahed, "An image-based multivariate generalized likelihood ratio control chart for detecting and diagnosing multiple faults in manufactured products," *Int. J. Prod. Res.*, vol. 54, no. 6, pp. 1771–1784, Mar. 2016.

[37] S. Knoth and W. Schmid, "Control charts for time series: A review," in *Frontiers in Statistical Quality Control*, vol. 7. Heidelberg, Germany: Springer, 2004.
[38] M. R. Reynolds and J. Lou, "An evaluation of a GLR control chart for monitoring the process mean," *J. Qual. Technol.*, vol. 42, no. 3, pp. 287–310, Jul. 2010.
[39] O. Bodnar and W. Schmid, "CUSUM charts for monitoring the mean of a multivariate Gaussian process," *J. Stat. Planning Inference*, vol. 141, no. 6, pp. 2055–2070, Jun. 2011.
[40] Z. Bai and H. Saranadasa, "Effect of high dimension: By an example of a two sample problem," *Statist. Sinica*, vol. 6, pp. 311–329, Apr. 1996.
[41] O. Ledoit and M. Wolf, "A well-conditioned estimator for large-dimensional covariance matrices," *J. Multivariate Anal.*, vol. 88, no. 2, pp. 365–411, Feb. 2004.
[42] E. Rafajłowicz, "Classifiers for matrix normal images: Derivation and testing," in *Proc. Int. Conf. Artif. Intell. Soft Comput.* Cham, Switzerland: Springer, 2018, pp. 668–679.
[43] S. X. Chen and Y.-L. Qin, "A two-sample test for high-dimensional data with applications to gene-set testing," *Ann. Statist.*, vol. 38, no. 2, pp. 808–835, Apr. 2010.
[44] A. M. Mathai and S. B. Provost, *Quadratic Forms in Random Variables: Theory and Applications*. New York, NY, USA: Dekker, 1992.

Yarema Okhrin received the M.S. degree (Hons.) in mathematics from the Ivan Franko National University of Lviv, Ukraine, in 1999, and the Ph.D. degree in economics and statistics *(summa cum laude)* from European University Viadrina, Frankfurt (Oder), Germany. He is currently a Professor of Statistics with the Faculty of Business and Economics, University of Augsburg, Germany. From April 2008 to September 2009, he was an Assistant Professor of Econometrics with the University of Bern, Switzerland. From March 2000 to March 2008, he was a Research Associate with the Department of Statistics, European University Viadrina, Frankfurt (Oder). His current research interests include financial econometrics, dependence modeling, analysis of image, networks, and environmental data. He is the Editor-in-Chief of "*Advances in Statistical Analysis*" and was the Vice-President of the German Statistical Society from 2012–2020.

Wolfgang Schmid received the M.S., Ph.D., and Habilitation degrees in mathematics from the University of Ulm, Germany, in 1982, 1984, and 1991, respectively. Since 1995, he has been a Full Professor of Statistics with European University Viadrina, Frankfurt (Oder), Germany. His main research activities include statistical analysis of financial markets, statistical process control, and statistical analysis of environmental processes. He is author of more than 150 publications, joint editor of the books "*Frontiers in Statistical Quality Control*" (Vol. 9–Vol. 12) and a primary supervisor of 25 dissertations. He is a member of the Editorial Board of "*AStA—Advances in Statistical Analysis*" and of the "*Journal of Multivariate Analysis*" and an Associate Editor of the journal "*Sequential Analysis*." He is an Elected Member of the International Statistical Institute, and he was the President of the German Statistical Society from 2012–2020.

Ivan Semeniuk received the B.S. and M.S. degrees in mathematics from the Taras Shevchenko National University of Kyiv, Kyiv, Ukraine, in 2014 and 2016, respectively. He is currently pursuing the Ph.D. degree with the Department of Statistics, European University Viadrina, Frankfurt (Oder), Germany. His current research interests include statistical process control for image processes, neural networks in statistical process control, and statistical approximation theory.